

## ■ Hydrogen Evolution | Very Important Paper |

VIP Polyoxometalate-Decorated g-C<sub>3</sub>N<sub>4</sub>-Wrapping Snowflake-Like CdS Nanocrystal for Enhanced Photocatalytic Hydrogen EvolutionXue-Li Zhai, Jiang Liu,\* Ling-Yun Hu, Jian-Chun Bao,\* and Ya-Qian Lan\*<sup>[a]</sup>

**Abstract:** Photocatalytic hydrogen evolution technology is recognized as a promising approach to relieving the growing energy crisis. Therefore, the development of a stable high-performance photocatalyst has long been the focus of research. In this work, quaternary composite materials involving a snowflake-like CdS nanocrystal wrapped by different amounts of polyoxometalate-decorated g-C<sub>3</sub>N<sub>4</sub> and polypyrrole (GPP@CdS) have been synthesized as photocatalysts for hydrogen production under visible-light irradiation. It has been revealed that the best composite (40% GPP@CdS composite) exhibits hydrogen production activity of 1321 μmol,

which exceeds that of CdS by a factor of more than two, and can be used in at least seven cycles with negligible loss of activity. The enhanced photocatalytic performance has been primarily attributed to the efficient synergy of CdS, g-C<sub>3</sub>N<sub>4</sub>, polypyrrole (PPy), and the polyoxometalate Ni<sub>4</sub>(PW<sub>9</sub>)<sub>2</sub>. It should be noted that the introduction of PPy and g-C<sub>3</sub>N<sub>4</sub> into the title composite simultaneously promotes electron/hole pair separation and photocatalytic stability, whereas Ni<sub>4</sub>(PW<sub>9</sub>)<sub>2</sub> serves as an efficient electron modulator and extra catalytic active site.


## Introduction

The continuous consumption of non-renewable energy sources and the large amounts of harmful gases released by burning fossil fuels have caused serious problems such as energy shortages and environmental pollution.<sup>[1–4]</sup> Therefore, the development of alternative energy sources to alleviate the above-mentioned crises has become a matter of urgency. Because hydrogen has the advantages of high combustion value, high efficiency, and no environmental pollution, the development of hydrogen energy has been recognized as one of most promising options for replacing non-renewable resources.<sup>[5–7]</sup> At present, hydrogen is mainly synthesized by electro- or photodriven water splitting.<sup>[8,9]</sup> Hydrogen evolution triggered by inexhaustible solar energy, with the assistance of a photocatalyst, has emerged as a popular strategy for investigation, because of the reduced energy consumption and cost.<sup>[10–12]</sup> In 1972, the semiconductor TiO<sub>2</sub> was first reported as a photocatalyst to split water.<sup>[13]</sup> Since then, hundreds of materials, including semiconductors,<sup>[14]</sup> heterojunctions,<sup>[15–17]</sup> and composite materials,<sup>[18–21]</sup> have been exploited to modulate the band gap of photocatalysts to further extend the light absorption range.

Among these materials, cadmium sulfide (CdS)<sup>[22–25]</sup> is considered to be a good visible-light photocatalyst due to its relatively narrow band gap (2.4 eV) and high-energy conduction band, which correspond to visible-light absorption. However, its photocatalytic activity is commonly confined by the rapid recombination of photogenerated carriers, light corrosion, and poor photocatalytic durability. So, the development of an efficient and stable photocatalyst is the key to producing hydrogen. Currently, composite materials have been widely used as a promising strategy in photocatalytic hydrogen production due to the synergistic effects of the components,<sup>[21,26,27]</sup> which can compensate the deficiency of a single component. Therefore, to effectively avoid the individual defects of CdS as a photocatalyst and to improve its photocatalytic activity, CdS combined with other materials has received increasing attention.<sup>[28]</sup> For instance, graphitic carbon nitride (g-C<sub>3</sub>N<sub>4</sub>)<sup>[29–33]</sup> has been combined with CdS to increase photocatalytic hydrogen production activity under visible-light irradiation, because its intrinsically tunable electronic structure, excellent stability, and fast charge-transfer ability can efficiently suppress the recombination of CdS photogenerated electron/hole pairs.<sup>[34]</sup> In parallel, polypyrrole (PPy), with a simple preparation, high electrical conductivity, and relatively low cost, has usually been integrated with CdS to boost the photocatalytic activity of the composite material by increasing its electron conductivity and stability.<sup>[35]</sup>

In addition to the above, the number of catalytic active sites on the surface of materials can greatly influence the photocatalytic activity. To further increase the number of active sites, polyoxometalates (POMs)<sup>[36–39]</sup> combined with CdS have been studied<sup>[40,41]</sup> due to their excellent redox properties and structural stability. However, POMs only have a response to ultraviolet

[a] X.-L. Zhai, Dr. J. Liu, L.-Y. Hu, Prof. Dr. J.-C. Bao, Prof. Dr. Y.-Q. Lan  
Jiangsu Collaborative Innovation Center  
of Biomedical Functional Materials  
School of Chemistry and Materials Science  
Nanjing Normal University, Nanjing 210023 (P. R. China)  
E-mail: liuj@njnu.edu.cn  
baojianchun@njnu.edu.cn  
yqlan@njnu.edu.cn

 Supporting information and the ORCID identification number(s) for the author(s) of this article can be found under:  
<https://doi.org/10.1002/chem.201803621>.

let light. Moreover, nearly naked polyoxometalates will lose their active ingredient if they are in prolonged contact with aqueous solutions, which strongly influences the stability of the target materials in photocatalytic hydrogen production.

In this work we have successfully prepared novel hybrid materials (GPP@CdS) that combine varying amounts of  $g\text{-C}_3\text{N}_4$ , PPy, and the POM  $\text{Ni}_4(\text{PW}_9)_2$  (see Figure S1 in the Supporting Information) with CdS by a convenient hydrothermal synthesis method. To evaluate the photocatalytic activities of the GPP@CdS composite materials, their behavior in photocatalytic hydrogen production was investigated. The results have revealed that the photocatalytic activities of the GPP@CdS composites are significantly promoted by the synergistic behavior of CdS,  $g\text{-C}_3\text{N}_4$ , PPy, and  $\text{Ni}_4(\text{PW}_9)_2$ . Specifically, 40% GPP@CdS displayed the highest hydrogen production activity of  $1321 \mu\text{mol}$ , which far surpasses that of pure CdS. Note that the improved separation of the photogenerated charges and electronic conductivity of the title composite material, which stem from the efficient cooperativity of the individual components, strongly enhance the activity and stability of this photocatalyst in hydrogen evolution.

## Results and Discussion

First, four GPP composites containing pyrrole,  $g\text{-C}_3\text{N}_4$ , and differing amounts of  $\text{Ni}_4(\text{PW}_9)_2$  were synthesized. The components and crystallographic structures of these precursor GPP composites were first investigated by powder X-ray diffraction (PXRD) and Raman spectroscopy. As shown in Figure S2 in the Supporting Information,  $g\text{-C}_3\text{N}_4$  displays characteristic diffraction peaks at  $13.1^\circ$  and  $27.3^\circ$ , which can be assigned to the approximate dimensions of the heptazine unit and the distance between graphitic layers.<sup>[7,42]</sup> In addition, the major diffraction peak at  $27.3^\circ$  of  $g\text{-C}_3\text{N}_4$  can be observed in the PXRD patterns of the GPP composites, but there is no clear characteristic diffraction peak at  $13.1^\circ$  because of the relatively low diffraction intensity of  $g\text{-C}_3\text{N}_4$ . At the same time, no characteristic diffraction peaks from  $\text{Ni}_4(\text{PW}_9)_2$  are observed in the PXRD patterns, which means that  $\text{Ni}_4(\text{PW}_9)_2$  is highly dispersed in the samples. To further ensure the compositions of the obtained GPP composites, they were characterized by Raman spectroscopy. In Figure S3 we can see the typical characteristic Raman peaks of  $g\text{-C}_3\text{N}_4$  with the presence of a D band located at around  $1340 \text{ cm}^{-1}$  and a G band at around  $1580 \text{ cm}^{-1}$ . The existence of D and G bands indicates that the composites indeed contain  $g\text{-C}_3\text{N}_4$ .<sup>[43]</sup> In addition, a group of bands with wavenumbers below  $1200 \text{ cm}^{-1}$  match well those of pure  $\text{Ni}_4(\text{PW}_9)_2$ , thereby evidencing that  $\text{Ni}_4(\text{PW}_9)_2$  molecules are successfully incorporated into the GPP composites.

The morphologies of the GPP composites were examined by transmission electron microscopy (TEM), which showed that  $g\text{-C}_3\text{N}_4$  possesses a thin sheet-like structure (see Figure S4a in the Supporting Information). With increasing content of  $\text{Ni}_4(\text{PW}_9)_2$ , more pyrrole molecules were oxidized into PPy to encapsulate the heteropoly-blue-decorated  $g\text{-C}_3\text{N}_4$  to yield a spherical morphology. As we can see in Figure S4b–e, agglomeration of the composites was gradually observed.

To further explore the morphologies and structures of these GPP composites, scanning electron microscope (SEM) images of GPP-0.1 (for the composition of GPP-0.1, see the Experimental Section) were obtained. As shown in Figure S5a, the SEM image clearly reveals that the spherical GPP-0.1 composite is uniform with an average size of approximately 100 nm, which is in good agreement with the TEM image. At the same time, the element distribution in GPP-0.1 was investigated by elemental mapping (see Figure S5b), which indicated that the elements carbon, nitrogen, oxygen, phosphorus, tungsten, and nickel are homogeneously distributed throughout the GPP-0.1 composite. The high-resolution TEM (HRTEM) image of the GPP-0.1 composite shows a clear lattice fringe (see Figure S6b) with a spacing of 3.36 nm, consistent with the (002) planes of  $g\text{-C}_3\text{N}_4$ , further evidence of the existence of  $g\text{-C}_3\text{N}_4$  in the GPP-0.1 composite.

Solid-state UV/Vis absorption spectra were recorded to verify the light-harvesting capability of these GPP composites. As shown in Figure S7 in the Supporting Information, all the GPP composites exhibit visible-light absorption and similar light-absorption edges at about 450 nm. However, their absorbance intensities are different; an increase in  $\text{Ni}_4(\text{PW}_9)_2$  content induces decreased light absorption intensity of the GPP composite, which can probably be attributed to increasing agglomeration of the samples and thus hindered absorption of incident light.

The photoproduction of hydrogen in the presence of the GPP composites as photocatalysts was evaluated by using an aqueous solution containing 0.35 M  $\text{Na}_2\text{S}$  and 0.25 M  $\text{Na}_2\text{SO}_3$  as sacrificial agents under visible-light irradiation ( $\lambda \geq 420 \text{ nm}$ ). As shown in Figure S8 in the Supporting Information, GPP-0.1 exhibits a relatively good hydrogen production performance of about  $37 \mu\text{mol}$  compared with the other GPP composites. Therefore, due to the good dispersion and relatively high photocatalytic activity of GPP-0.1, the title composite materials incorporating CdS (GPP@CdS) were synthesized by using GPP-0.1 as precursor.

The GPP@CdS composites were synthesized through a facile one-pot hydrothermal method (see the Experimental Section for details). The crystalline structures of the GPP@CdS composites were characterized by PXRD, and their patterns are compared with those of pure  $g\text{-C}_3\text{N}_4$ ,  $\text{Ni}_4(\text{PW}_9)_2$ , and CdS in Figure 1e. The PXRD patterns of the GPP@CdS composites synthesized with different contents of GPP-0.1 show a group of strong diffraction peaks below  $35^\circ$  that partially match the signals of pure  $\text{Ni}_4(\text{PW}_9)_2$ , which proves the existence of  $\text{Ni}_4(\text{PW}_9)_2$ . Moreover, all the diffraction peaks marked with a blue circle can be indexed to the (100), (002), (101), (102), (110), (103), (112), and (201) planes of the hexagonal phase CdS (JCPDS 75-1545, Figure 1e). However, none of the GPP@CdS composites show characteristic diffraction peaks for carbon species in the PXRD patterns because of the low amount and relatively low diffraction intensity of  $g\text{-C}_3\text{N}_4$ . Furthermore, the results indicate that the introduction of  $\text{Ni}_4(\text{PW}_9)_2$ , PPy, and  $g\text{-C}_3\text{N}_4$  has no effect on the crystalline phase of CdS.

The morphologies of pure CdS and the GPP@CdS composites were characterized by TEM and SEM. As shown in Figure S9 in the Supporting Information, the TEM images reveal

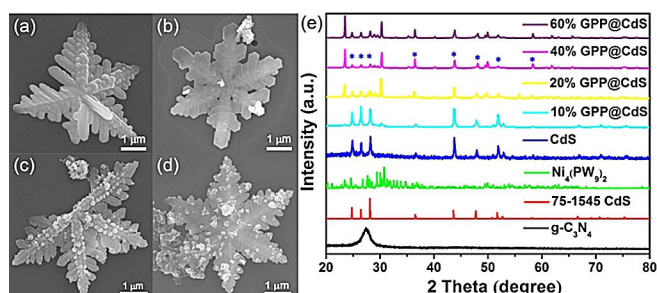


**Figure 1.** SEM images of (a) 10% GPP@CdS, (b) 20% GPP@CdS, (c) 40% GPP@CdS, and (d) 60% GPP@CdS. (e) PXRD patterns of g-C<sub>3</sub>N<sub>4</sub>, Ni<sub>4</sub>(PW<sub>9</sub>)<sub>2</sub>, pure CdS, 10% GPP@CdS, 20% GPP@CdS, 40% GPP@CdS, and 60% GPP@CdS.

that the individual CdS has a dendrimer-like morphology with a particle size of approximately 3–4 μm, and that with increasing precursor content, the GPP@CdS composites acquire a snowflake-like morphology with particle diameters of approximately 3–7 μm. Furthermore, these morphological features of the GPP@CdS composites were also evidenced by SEM (Figure 1a–d). As we can see, the 40% GPP@CdS composite displays seemingly appropriate loadings of the GPP precursor, whereas the other composites (10, 20, and 60%) embrace less or more loadings, which results in aggregation phenomenon. Moreover, the relatively moderate GPP precursor distribution in the 40% GPP@CdS composite can be corroborated by selecting different areas of the material surface in the TEM and HRTEM images. Further close inspection revealed detailed structural information on 40% GPP@CdS (Figure 2 and Figure S10). In the HRTEM image of 40% GPP@CdS in Figure 2b, clear lattice fringes with spacings of 0.36 and 2.61 nm are observed, which correspond to the (100) planes of the hexagonal phase CdS (JCPDS 75-1545) and (102) planes of g-C<sub>3</sub>N<sub>4</sub>. In addition, the selected-area electron diffraction (SAED) pattern (inset in Figure 2a) evidences the presence of hexagonal cadmium sulfide in the GPP@CdS composites. As revealed in Figure 2c, high-angle annular dark-field scanning transition electron microscopy (HAADF-STEM) and elemental mapping show that

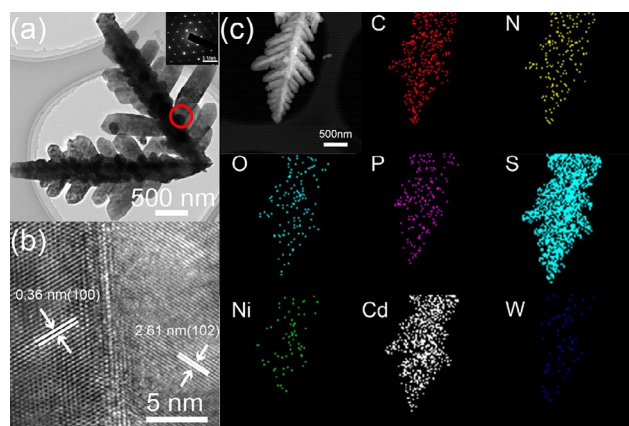


**Figure 2.** (a) TEM image and SEAD patterns, (b) HRTEM image, and (c) dark-field STEM image and the corresponding energy-dispersive X-ray spectroscopy (EDS) mapping of 40% GPP@CdS.

the elements carbon, nitrogen, oxygen, phosphorus, tungsten, nickel, sulfur, and cadmium are homogeneously distributed throughout the whole of the 40% GPP@CdS composite material, which is a polyoxometalate-decorated g-C<sub>3</sub>N<sub>4</sub>-wrapping snowflake-like CdS nanocrystal material.

From the FTIR spectra of pure g-C<sub>3</sub>N<sub>4</sub>, Ni<sub>4</sub>(PW<sub>9</sub>)<sub>2</sub>, GPP-0.1, and the 40% GPP@CdS composite (see Figure S11 in the Supporting Information), it can be seen that the spectrum of the 40% GPP@CdS sample shows features that are also observed in the spectra of pure g-C<sub>3</sub>N<sub>4</sub> and Ni<sub>4</sub>(PW<sub>9</sub>)<sub>2</sub>. The sharp absorption band at 805 cm<sup>-1</sup> is a bending vibration characteristic of the tri-s-triazine units constituting g-C<sub>3</sub>N<sub>4</sub>.<sup>[44]</sup> The strong absorption peaks in the range of 1200–1600 cm<sup>-1</sup> belong to the characteristic stretching vibration modes of heterocyclic C=N and C–N.<sup>[44]</sup> Thus, it is further demonstrated that the 40% GPP@CdS sample contains g-C<sub>3</sub>N<sub>4</sub>. At the same time, the FTIR spectrum of 40% GPP@CdS shows bands very similar to those observed in the spectrum of Ni<sub>4</sub>(PW<sub>9</sub>)<sub>2</sub>, which demonstrates that the structure of Ni<sub>4</sub>(PW<sub>9</sub>)<sub>2</sub> is maintained within the composite.

To further confirm the compositions of the acquired GPP@CdS composites, their Raman spectra were also recorded. As displayed in Figure S3 in the Supporting Information, the Raman spectrum of pure CdS displays Raman peaks at 295 and 604 cm<sup>-1</sup>.<sup>[45]</sup> With regard to the 40% GPP@CdS composite, the Raman spectrum exhibits characteristic peaks of g-C<sub>3</sub>N<sub>4</sub> and CdS. No obvious Raman peak of Ni<sub>4</sub>(PW<sub>9</sub>)<sub>2</sub> can be observed in the spectrum of the 40% GPP@CdS composite, which is probably due to the relatively weak intensity of Ni<sub>4</sub>(PW<sub>9</sub>)<sub>2</sub> in the composite sample. Therefore, the Raman spectrum provides further evidence for the formation of the 40% GPP@CdS composite.

X-ray photoelectron spectroscopy (XPS) was used to identify the atomic valence states and chemical compositions. Figure 3 displays the high-resolution XPS spectra of the elements C 1s, N 1s, Cd 3d, S 2p, P 2p, and W 4f for the 40% GPP@CdS sample. Clearly, the C 1s peak in Figure 3a can be separated into three peaks with binding energies of 284.8, 287.5, and 290.0 eV. The strongest peak at 284.8 eV can be assigned to the graphite carbon in g-C<sub>3</sub>N<sub>4</sub>, and the other two peaks at 287.5 and 290.0 eV originate from the C–N–C and C–N bonds, respectively.<sup>[46,47]</sup> The N 1s spectrum presents two peaks at 398.4 and 399.6 eV (Figure 3b), which have been assigned to pyridinic and tertiary nitrogen (N–(C)<sub>3</sub>), respectively.<sup>[32,48]</sup> The presence of C 1s and N 1s in the XPS spectra further proves that g-C<sub>3</sub>N<sub>4</sub> and PPy exist in the 40% GPP@CdS composite. The P 2p spectrum presents two peaks at 133.1 and 134.5 eV (Figure 3c), which can be attributed to P–C and P–O bonds, respectively.<sup>[48]</sup> Figure 3d shows characteristic peaks at 35.6 and 37.8 eV for W 4f, which correspond to W 4f 5/2 and W 4f 7/2, respectively. Hence, the XPS spectra of both P 2p and W 4f demonstrate the existence of Ni<sub>4</sub>(PW<sub>9</sub>)<sub>2</sub> in the composite. Additionally, the characteristic binding energies of Cd 3d are observed at 405.1 and 411.9 eV (Figure 3e), which correspond to Cd 3d 3/2 and Cd 3d 5/2 and suggests that the chemical state of the cadmium element in the 40% GPP@CdS sample is Cd<sup>2+</sup>.<sup>[46]</sup> S 2p 1/2 and 2p 3/2 peaks are detected at binding energies of 162.7 and 161.5 eV (Figure 3f), which have been assigned to S<sup>2-</sup>, and this result is in good agreement with the chemical



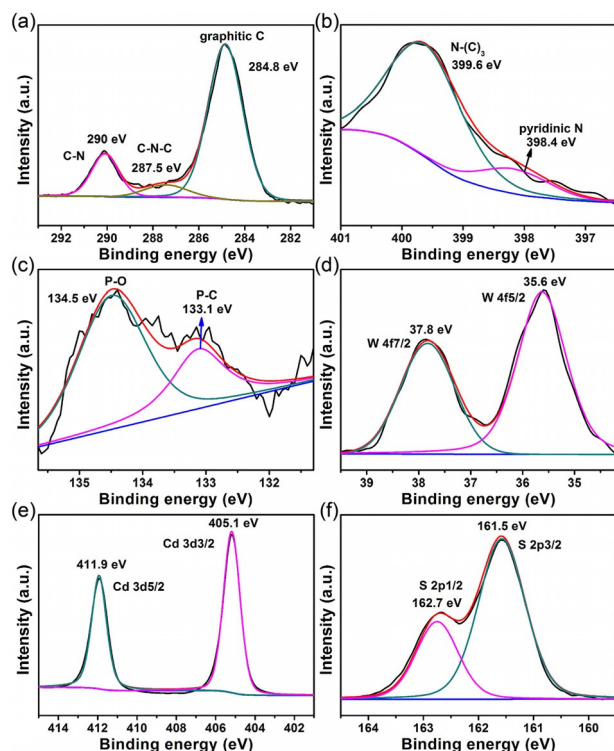


**Figure 3.** XPS spectra of (a) C 1s, (b) N 1s, (c) P 2p, (d) W 4f, (e) Cd 3d, and (f) S 2p electrons of the 40% GPP@CdS composite.

state of the sulfur element in the 40% GPP@CdS sample.<sup>[46]</sup> Thus, these results suggest that the GPP@CdS composite photocatalyst was successfully synthesized by our approach.

The photocatalytic performances of CdS, CdS/g-C<sub>3</sub>N<sub>4</sub>, and the GPP@CdS composites in H<sub>2</sub> production were evaluated under visible-light ( $\lambda \geq 420$  nm) irradiation in the presence of a sacrificial electron donor composed of Na<sub>2</sub>S (0.25 M) and Na<sub>2</sub>SO<sub>3</sub> (0.35 M). From Figure 4a we can see that the GPP-0.1 composite wrapping CdS plays an extremely important role in improving the photocatalytic activity. It is well known that pure CdS displays relatively low H<sub>2</sub> production activity, because of the easy recombination of photogenerated hole/electron pairs. Although a certain amount of g-C<sub>3</sub>N<sub>4</sub> incorporated into pure CdS improves the photocatalytic hydrogen evolution, the 40% GPP@CdS composite displays the highest hydrogen production activity of 1321  $\mu\text{mol}$ , which exceeds that of CdS/g-

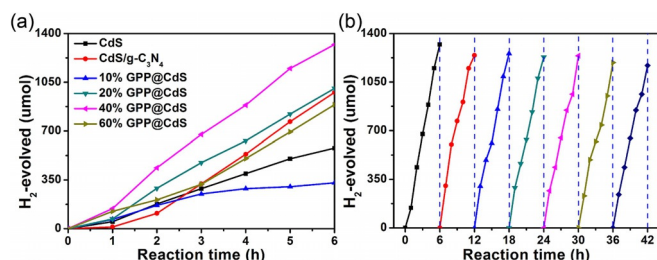


**Figure 4.** (a) Photocatalytic H<sub>2</sub> production activity of different samples in a vacuum under visible-light irradiation ( $\lambda \geq 420$  nm) and (b) photocatalytic stability of the 40% GPP@CdS composite in a vacuum under visible-light irradiation ( $\lambda \geq 420$  nm).

C<sub>3</sub>N<sub>4</sub> and pure CdS. In contrast to other POM-based photocatalysts (see Table S1 in the Supporting Information), it is clear that the 40% GPP@CdS in this study shows a much better photocatalytic performance. Moreover, the photocatalytic performance of the GPP@CdS composites decreases with a further increase of GPP-0.1 content, probably because the introduction of a large percentage of GPP composites would result in aggregation and shield the active sites on the CdS surface, as shown in Figure 1d. As a consequence, a suitable content of GPP composite coating is essential to improve the photocatalytic activity of the GPP@CdS composite materials.

Cadmium sulfide is susceptible to light corrosion and their short lifetimes are their most serious drawback. Therefore, the photocatalytic durability and stability of our composites were also investigated. As revealed in Figure 4b, the photocatalytic performance of 40% GPP@CdS in H<sub>2</sub> production did not undergo any obvious decline after seven cycles of 6 h, which proves that our composite has extremely good photocatalytic stability during the photocatalytic reaction. Moreover, the stability of the 40% GPP@CdS composite was further confirmed by its PXRD pattern and FTIR spectrum after the photocatalytic reactions (see Figures S13 and S14 in the Supporting Information). In addition, the TEM images of the system after the photocatalytic reaction show no noticeable g-C<sub>3</sub>N<sub>4</sub> and/or other deciduous active components (see Figure S15). Such high-performance photocatalytic activity and stability can mainly be attributed to the synergy of the multicomponent contributions. On the one hand, the wrapped polyoxometalate-decorated g-C<sub>3</sub>N<sub>4</sub> sheets effectively suppress the recombination of the photogenerated carriers of CdS and further provide more photoactive sites. On the other hand, the formation of PPy weakens the possibility of loss of the composite active components through its packaging capacity. Hence, we propose the photocatalytic reaction mechanism shown in Figure 5.

In addition, the title GPP@CdS composites show extended solid-state UV/Vis absorption spectra, as displayed in Figure S16a in the Supporting Information. It can be seen that all the GPP@CdS composites have a similar light absorption edge at about 550 nm, and all have overwhelmingly higher absorption intensities than pure CdS. Therefore, we can infer that the GPP@CdS composites utilize solar energy more efficiently. Moreover, according to the Kubelka–Munk approximation for calculating band gaps, as shown in Figure S16b, the band gap of 40% GPP@CdS is 2.31 eV, which is also lower than that of CdS.

To further prove that 40% GPP@CdS is the best photocatalyst of our composites, the photoelectrochemical properties were investigated through photocurrent measurements and electrochemical impedance spectroscopy (EIS). Figure S17a in the Supporting Information shows that all the composites display clear photocurrent responses under visible-light irradiation, but 40% GPP@CdS exhibits a much higher photocurrent than 10, 20, and 60% GPP@CdS and thus demonstrates the good separation efficiency of the photoinduced electron/hole pairs for the sample 40% GPP@CdS.

Electrochemical impedance spectroscopy (EIS) is a useful tool for the characterization of semiconductor carrier mobility.

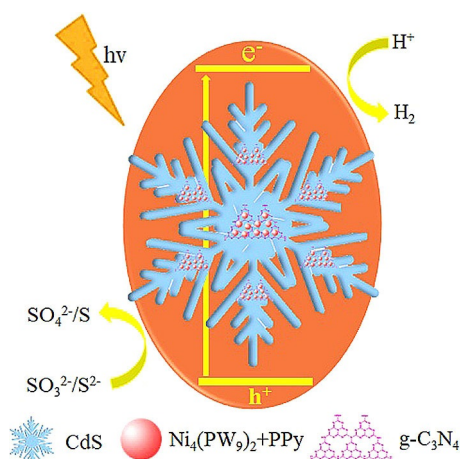


**Figure 5.** Photocatalytic mechanism of the GPP@CdS composites under visible-light irradiation.

Thus, rapid charge transport in the GPP@CdS composites was confirmed by electrochemical impedance spectra (EIS). As can be seen in Figure S18 in the Supporting Information, 40% GPP@CdS exhibits the smallest semicircle, which indicates the fastest interfacial charge transfer, which is also in agreement with the above photocurrent response results. Additionally, the steady-state photoluminescence (PL) emission spectra of CdS and the GPP@CdS composites were recorded under an excitation wavelength of 460 nm (see Figure S17b). The PL intensities of the prepared GPP@CdS composites are clearly weaker than that of pure CdS. Furthermore, the lowest PL intensity observed for the 40% GPP@CdS composite suggests accelerated separation of the photoexcited electrons and holes. Thus, all these facts indicate that the 40% GPP@CdS composite is an excellent catalyst with high photocatalytic activity.

## Conclusion

A novel polyoxometalate-decorated g-C<sub>3</sub>N<sub>4</sub>-wrapping snowflake-like CdS nanocrystal photocatalyst has been synthesized by a convenient hydrothermal synthesis method. The nanohybrid of 40% GPP@CdS displays high-performance hydrogen production activity and superior photocatalytic stability. It is noted that the introduction of the Ni<sub>4</sub>(PW<sub>9</sub>)<sub>2</sub> POM into the hybrid not only acts as a redox electron modulator, but also as a co-catalyst in the photocatalytic reaction. Additionally, our findings show that the synergistic effect derived from multi-component contributions can effectively enhance the activity in photocatalytic hydrogen evolution, and that this work offers a broad prospect for exploring polynary photocatalytic composite materials.

## Experimental Section

**Chemicals:** Sodium tungstate dehydrate (Na<sub>2</sub>WO<sub>4</sub>·2H<sub>2</sub>O), disodium hydrogen phosphate dodecahydrate (Na<sub>2</sub>HPO<sub>4</sub>), acetic acid (CH<sub>3</sub>COOH), cadmium nitrate (Cd(NO<sub>3</sub>)<sub>2</sub>·4H<sub>2</sub>O), nickel acetate tetrahydrate (C<sub>4</sub>H<sub>6</sub>O<sub>4</sub>Ni·4H<sub>2</sub>O), pyrrole (C<sub>4</sub>H<sub>5</sub>N), anhydrous sodium sulfate (Na<sub>2</sub>SO<sub>3</sub>), and anhydrous ethanol (C<sub>2</sub>H<sub>5</sub>OH) were purchased

from Sinopharm Chemical Reagent Co. Ltd. (Shanghai). Dicyandiamide (C<sub>2</sub>H<sub>4</sub>N<sub>4</sub>), thiourea (CH<sub>4</sub>N<sub>2</sub>S), and potassium acetate (C<sub>2</sub>H<sub>3</sub>KO<sub>2</sub>) were purchased from Shanghai Lingfeng Chemical Co. Ltd. Sodium sulfide nonahydrate (Na<sub>2</sub>S·9H<sub>2</sub>O) was purchased from Aladdin (Shanghai). Unless noted otherwise, all chemicals were used without further purification. Deionized water (18.2 MΩ) was prepared by using a pure power water purification system (Yaoling, China).

**Synthesis of pure CdS:** Pure CdS was synthesized according to a modified literature method.<sup>[49]</sup> Cd(NO<sub>3</sub>)<sub>2</sub>·4H<sub>2</sub>O and thiourea in a ratio of 2:1 were dissolved in deionized water (10 mL) and the mixture was stirred at room temperature for 30 min. After stirring, the solution was subsequently transferred into a 12 mL Teflon-lined autoclave and heated at 220 °C for 18 h. After cooling, the product was collected by centrifugation and washed three times with distilled water and anhydrous ethanol, respectively, and the resulting material was vacuum-dried overnight at 60 °C.

**Synthesis of g-C<sub>3</sub>N<sub>4</sub>:** g-C<sub>3</sub>N<sub>4</sub> was prepared by the thermal polycondensation of dicyandiamide as follows: Dicyandiamide powder (5 g) was placed in a porcelain boat and heated from 25 to 550 °C in air over 3 h at a heating rate of 3 °C min<sup>-1</sup>, and then maintained at this temperature for 4 h. The obtained yellow product was collected and ground to a powder for further use.

**Synthesis of polyanion [Ni<sub>4</sub>(H<sub>2</sub>O)<sub>2</sub>(PW<sub>9</sub>O<sub>34</sub>)<sub>2</sub>]<sup>10-</sup>:** Na<sub>6</sub>K<sub>4</sub>[Ni<sub>4</sub>(H<sub>2</sub>O)<sub>2</sub>(PW<sub>9</sub>O<sub>34</sub>)<sub>2</sub>]<sub>2</sub>·32H<sub>2</sub>O (Ni<sub>4</sub>(PW<sub>9</sub>)<sub>2</sub>) was synthesized according to a reported procedure.<sup>[50]</sup> Na<sub>2</sub>WO<sub>4</sub>·2H<sub>2</sub>O (33 g, 100 mmol) and Na<sub>2</sub>HPO<sub>4</sub> (1.57 g, 11 mmol) were dissolved in deionized water (100 mL) and the mixture stirred well. The pH of the solution was then adjusted to about 7.0 with acetic acid. This solution was slowly added to a solution of C<sub>4</sub>H<sub>6</sub>O<sub>4</sub>Ni·4H<sub>2</sub>O (5.5 g, 22 mmol) in deionized water (50 mL) under vigorous magnetic stirring. The resulting mixture was heated at reflux for 2.5 h and then filtered to remove any precipitate. Then C<sub>2</sub>H<sub>3</sub>KO<sub>2</sub> (4 g) was added and stirred until it had completely dissolved and a yellow solution was obtained. The desired product was collected as a mixture of small high-quality yellow crystals and a crystalline powder by filtration.

**Synthesis of CdS/g-C<sub>3</sub>N<sub>4</sub>:** CdS/g-C<sub>3</sub>N<sub>4</sub> was obtained by a one-pot hydrothermal method as follows. Cd(NO<sub>3</sub>)<sub>2</sub>·4H<sub>2</sub>O and thiourea in a ratio of 2:1 were dissolved in deionized water (10 mL), and then g-C<sub>3</sub>N<sub>4</sub> (8.5 mg) was added and the mixture stirred at room temperature for 30 min. Finally, the solution was subsequently transferred into a 12 mL Teflon-lined autoclave and heated at 220 °C for 18 h. After cooling, the product was collected by centrifugation and then washed three times with distilled water and anhydrous ethanol, respectively. The resulting material (CdS/g-C<sub>3</sub>N<sub>4</sub>) was placed in a vacuum oven and dried at 60 °C.

**Synthesis of the Ni<sub>4</sub>(PW<sub>9</sub>)<sub>2</sub>, pyrrole, and g-C<sub>3</sub>N<sub>4</sub> composite (GPP):** Ni<sub>4</sub>(PW<sub>9</sub>)<sub>2</sub> (0.05 mmol) and pyrrole (Py; 100 μL) were dissolved in deionized water (30 mL) and the mixture stirred for 30 min. Then g-C<sub>3</sub>N<sub>4</sub> (150 mg) was added and a grayish yellow solution was observed after stirring for 60 min. The solution was subsequently transferred into a 50 mL Teflon-lined autoclave and heated at 110 °C for 18 h. After cooling, the resulting product (GPP-0.05) was separated by centrifugation and washed three times with distilled water and anhydrous ethanol, respectively. The resulting product was placed in a vacuum oven and dried at 60 °C overnight. Under the same conditions, the reaction was repeated by using 0.1, 0.2, and 0.5 mmol of Ni<sub>4</sub>(PW<sub>9</sub>)<sub>2</sub> to yield GPP-0.1, GPP-0.2, and GPP-0.5, respectively.

**Synthesis of the CdS and GPP composite (GPP@CdS):** Cd(NO<sub>3</sub>)<sub>2</sub>·4H<sub>2</sub>O and thiourea in a ratio of 2:1 were dissolved in deionized water (10 mL) and the mixture stirred at room temperature for 30 min. A series of composite materials, abbreviated as 10%

GPP@CdS, 20% GPP@CdS, 40% GPP@CdS, and 60% GPP@CdS, were synthesized by adding different amounts of GPP-0.1, the quantities of which gave total mass fractions of 10, 20, 40, and 60% GPP, respectively. The resulting solutions were stirred for 1 h and then transferred into a 12 mL Teflon-lined autoclave and heated at 220 °C for 18 h. After cooling, the products were collected by centrifugation. The final products were washed three times with distilled water and anhydrous ethanol, respectively. The obtained materials were placed in a vacuum oven and dried at 60 °C.

**Materials characterization:** The PXRD patterns of the dried products were recorded on a D/max 2500 VL/PC diffractometer (Japan) using  $\text{Cu}_{\text{K}\alpha}$  irradiation ( $\lambda = 1.54060 \text{ \AA}$ ) and an operating voltage and current of 40 kV and 100 mA, respectively. TEM characterization was performed with a JEM-200CX instrument (Japan) using an accelerating voltage of 200 kV. HRTEM images were obtained with a JEOL-2100F apparatus at an accelerating voltage of 200 kV, and was equipped with an elemental mapping device, scanning transmission electron microscope (STEM), and high-angle annular dark-field scanning TEM (HAADF-STEM). Electrochemical impedance spectra were recorded by using a three-electrode system (platinum electrode as the counter electrode and Ag/AgCl as the reference electrode) over a frequency range of 1 Hz to 100 kHz with an ac amplitude of 10 mV at 0.5 V. A solution of  $\text{Na}_2\text{S}$  (0.1 M) and  $\text{Na}_2\text{SO}_3$  (0.02 M) was used as the supporting electrolyte. FTIR spectra were recorded on a Nexus 670 spectrometer. UV/Vis absorption and diffuse reflectance spectra were recorded on a Cary 5000 UV/Vis spectrometer (Varian, USA) by using pure  $\text{BaSO}_4$  as the reference sample. The thermogravimetric data were collected on a TGA NETZSCH STA449F3 instrument. Photoelectrochemical (PEC) measurements were performed on a Zahner PEC workstation (Zahner, Germany). Photoluminescence (PL) spectra were recorded on a Fluoromax-4 spectrofluorimeter (Horiba, USA). The X-ray photoelectron spectra were acquired on a Thermo ESCALAB 250Xi X-ray photoelectron spectrometer by using  $\text{Al}_{\text{K}\alpha}$  radiation. The binding energy of the C 1s peak (284.6 eV) was employed as a standard to calibrate the binding energies of the other elements.

**Photocatalytic activity tests:** The photocatalytic water splitting reactions were carried out in a fully enclosed gas circulation system (CEL-SPH2N, CEALight, China) in a 300 mL Pyrex flask, the openings which were sealed with silicone rubber septa. All glassware was rinsed with deionized water prior to use. The light source was a 300 W xenon arc lamp and a cutoff filter with a wavelength range of 420–800 nm was used. The amount of  $\text{H}_2$  evolved was analyzed by gas chromatography (GC-7900, CEALight, China). The as-prepared photocatalyst powder (5 mg) was dispersed in an aqueous solution (100 mL) of 0.35 M  $\text{Na}_2\text{SO}_3$  and 0.25 M  $\text{Na}_2\text{S}$  as sacrificial reagents. Before irradiation, the system was degassed by evacuation to remove any dissolved oxygen and ensure the reactor was in anaerobic conditions. The released hydrogen gas was determined by gas chromatography. The photocatalytic stability was investigated under the same conditions. The sacrificial agents were refreshed every 6 h to assess the photocatalytic stability in a vacuum.

## Acknowledgements

We thank the National Natural Science Foundation of China (No. 21471081, 21533012, 21622104, 21471080 and 21701085), the NSF of Jiangsu Province of China (No. BK20171032), and the Natural Science Research of Jiangsu Higher Education Institutions of China (No. 17KJB150025) for financial support.

## Conflict of interest

The authors declare no conflict of interest.

**Keywords:** composite materials • hydrogen • photocatalysis • synergistic effects • water splitting

- [1] G. X. Zhao, Y. B. Sun, W. Zhou, X. K. Wang, K. Chang, G. G. Liu, H. M. Liu, T. Kako, J. H. Ye, *Adv. Mater.* **2017**, *29*, 1703258.
- [2] H. J. Yan, J. H. Yang, G. J. Ma, G. P. Wu, X. Zong, Z. B. Lei, J. Y. Shi, C. Li, *J. Catal.* **2009**, *266*, 165–168.
- [3] J. L. Meng, Z. M. Yu, Y. Li, Y. D. Li, *Catal. Today* **2014**, *225*, 136–141.
- [4] W. Iqbal, C. Y. Dong, M. Y. Xing, X. J. Tan, J. L. Zhang, *Catal. Sci. Technol.* **2017**, *7*, 1726–1734.
- [5] G. C. Xie, K. Zhang, B. D. Guo, Q. Liu, L. Fang, J. R. Gong, *Adv. Mater.* **2013**, *25*, 3820–3839.
- [6] Q. Li, B. D. Guo, J. G. Yu, J. R. Ran, B. H. Zhang, H. J. Yan, J. R. Gong, *J. Am. Chem. Soc.* **2011**, *133*, 10878–10884.
- [7] F. Dong, Z. W. Zhao, T. Xiong, Z. L. Ni, W. D. Zhang, Y. J. Sun, W. K. Ho, *ACS Appl. Mater. Interfaces* **2013**, *5*, 11392–11401.
- [8] B. C. Qiu, Q. H. Zhu, M. M. Du, L. G. Fan, M. Y. Xing, J. L. Zhang, *Angew. Chem. Int. Ed.* **2017**, *56*, 2684–2688; *Angew. Chem.* **2017**, *129*, 2728–2732.
- [9] R. Liu, Z. Zheng, J. Spurgeon, X. G. Yang, *Energy Environ. Sci.* **2014**, *7*, 2504–2517.
- [10] Y. P. Xie, Z. B. Yu, G. Liu, X. L. Ma, H. M. Cheng, *Energy Environ. Sci.* **2014**, *7*, 1895–1901.
- [11] T. Takata, C. S. Pan, M. Nakabayashi, N. Shibata, K. Domen, *J. Am. Chem. Soc.* **2015**, *137*, 9627–9634.
- [12] H. N. Kim, T. W. Kim, I. Y. Kim, S. J. Hwang, *Adv. Funct. Mater.* **2011**, *21*, 3111–3118.
- [13] A. Fujishima, K. Honda, *Nature* **1972**, *238*, 37–38.
- [14] T. A. Kandiel, I. Ivanova, D. W. Bahnemann, *Energy Environ. Sci.* **2014**, *7*, 1420–1425.
- [15] X. W. Wang, L. C. Yin, G. Liu, L. Z. Wang, R. Saito, G. Q. Lu, H. M. Cheng, *Energy Environ. Sci.* **2011**, *4*, 3976–3979.
- [16] X. W. Wang, G. Liu, Z. G. Chen, F. Li, L. Z. Wang, G. Q. Lu, H. M. Cheng, *Chem. Commun.* **2009**, 3452–3454.
- [17] J. X. Low, J. G. Yu, M. Jaroniec, S. Wageh, A. A. Al-Ghamdi, *Adv. Mater.* **2017**, *29*, 1601694.
- [18] Y. Y. Chen, M. Han, Y. J. Tang, J. C. Bao, S. L. Li, Y. Q. Lan, Z. H. Dai, *Chem. Commun.* **2015**, *51*, 12377–12380.
- [19] T. F. Wu, P. F. Wang, J. Qian, Y. H. Ao, C. Wang, J. Hou, *Dalton Trans.* **2017**, *46*, 13793–13801.
- [20] Q. Li, X. Li, S. Wageh, A. A. Al-Ghamdi, J. G. Yu, *Adv. Energy Mater.* **2015**, *5*, 1500010.
- [21] Z. Q. Jiang, J. X. Liu, M. Y. Gao, X. Fan, L. Zhang, J. Zhang, *Adv. Mater.* **2017**, *29*, 1603369.
- [22] L. Shang, B. Tong, H. J. Yu, G. I. N. Waterhouse, C. Zhou, Y. F. Zhao, M. Tahir, L. Z. Wu, C. H. Tung, T. R. Zhang, *Adv. Energy Mater.* **2016**, *6*, 1501241.
- [23] Z. F. Zhang, Y. S. Ren, L. Han, G. Y. Xie, B. Zhong, *Physica E* **2017**, *92*, 30–35.
- [24] M. H. Luo, W. F. Yao, C. P. Huang, Q. Wu, Q. J. Xu, *J. Mater. Chem. A* **2015**, *3*, 13884–13891.
- [25] Y. Hu, X. H. Gao, L. Yu, Y. R. Wang, J. Q. Ning, S. J. Xu, X. W. Lou, *Angew. Chem. Int. Ed.* **2013**, *52*, 5636–5639; *Angew. Chem.* **2013**, *125*, 5746–5749.
- [26] X. L. Xing, R. J. Liu, X. L. Yu, G. J. Zhang, H. B. Cao, J. N. Yao, B. Z. Ren, Z. X. Jiang, H. Zhao, *J. Mater. Chem. A* **2013**, *1*, 1488–1494.
- [27] W. W. Guo, H. J. Lv, Z. Y. Chen, K. P. Sullivan, S. M. Lauinger, Y. N. Chi, J. M. Sumliner, T. Q. Lian, C. L. Hill, *J. Mater. Chem. A* **2016**, *4*, 5952–5957.
- [28] P. P. Bag, X. S. Wang, P. Sahoo, J. H. Xiong, R. Cao, *Catal. Sci. Technol.* **2017**, *7*, 5113–5119.
- [29] Y. Zheng, L. H. Lin, B. Wang, X. C. Wang, *Angew. Chem. Int. Ed.* **2015**, *54*, 12868–12884; *Angew. Chem.* **2015**, *127*, 13060–13077.



- [30] G. X. Zhao, X. B. Huang, F. Fina, G. Zhang, J. T. S. Irvine, *Catal. Sci. Technol.* **2015**, *5*, 3416–3422.
- [31] Z. W. Zhao, Y. J. Sun, F. Dong, *Nanoscale* **2015**, *7*, 15–37.
- [32] G. G. Zhang, M. W. Zhang, X. X. Ye, X. Q. Qiu, S. Lin, X. C. Wang, *Adv. Mater.* **2014**, *26*, 805–809.
- [33] Y. F. Li, R. X. Jin, Y. Xing, J. Q. Li, S. Y. Song, X. C. Liu, M. Li, R. C. Jin, *Adv. Energy Mater.* **2016**, *6*, 1601273.
- [34] L. Ge, F. Zuo, J. K. Liu, Q. Ma, C. Wang, D. Z. Sun, L. Bartels, P. Y. Feng, *J. Phys. Chem. C* **2012**, *116*, 13708–13714.
- [35] Y. R. Shan, J. Zhao, W. J. Li, Q. L. Huang, C. F. Xiao, *J. Mater. Sci.* **2018**, *53*, 2065–2076.
- [36] J. Q. Shen, Y. Zhang, Z. M. Zhang, Y. G. Li, Y. Q. Gao, E. B. Wang, *Chem. Commun.* **2014**, *50*, 6017–6019.
- [37] M. Murakami, D. C. Hong, T. Suenobu, S. Yamaguchi, T. Ogura, S. Fukuzumi, *J. Am. Chem. Soc.* **2011**, *133*, 11605–11613.
- [38] H. J. Lv, Y. Z. Gao, W. W. Guo, S. M. Lauinger, Y. N. Chi, J. Bacsá, K. P. Sullivan, M. Wieliczko, D. G. Musaev, C. L. Hill, *Inorg. Chem.* **2016**, *55*, 6750–6758.
- [39] Y. Q. Jiao, C. Qin, X. L. Wang, F. H. Liu, P. Huang, C. G. Wang, K. Z. Shao, Z. M. Su, *Chem. Commun.* **2014**, *50*, 5961–5963.
- [40] X. L. Yu, R. J. Liu, G. J. Zhang, *RSC Adv.* **2013**, *3*, 8351–8355.
- [41] M. Wang, X. K. Shang, X. L. Yu, R. J. Liu, Y. B. Xie, H. Zhao, H. B. Cao, G. J. Zhang, *Phys. Chem. Chem. Phys.* **2014**, *16*, 26016–26023.
- [42] D. J. Martin, P. J. T. Reardon, S. J. A. Moniz, J. W. Tang, *J. Am. Chem. Soc.* **2014**, *136*, 12568–12571.
- [43] Q. Liu, J. Y. Zhang, *Langmuir* **2013**, *29*, 3821–3828.
- [44] M. S. Akple, J. Low, S. Wageh, A. A. Al-Ghamdi, J. G. Yu, J. Zhang, *Appl. Surf. Sci.* **2015**, *358*, 196–203.
- [45] C. Han, Z. Chen, N. Zhang, J. C. Colmenares, Y. J. Xu, *Adv. Funct. Mater.* **2015**, *25*, 221–229.
- [46] X. J. Ye, X. Dai, S. G. Meng, X. L. Fu, S. F. Chen, *Chin. J. Chem.* **2017**, *35*, 217–225.
- [47] K. Zhang, M. Park, J. Zhang, G. H. Lee, J. Shin, Y. M. Kang, *Nano Res.* **2017**, *10*, 4337–4350.
- [48] J. S. Li, Y. Wang, C. H. Liu, S. L. Li, Y. G. Wang, L. Z. Dong, Z. H. Dai, Y. F. Li, Y. Q. Lan, *Nat. Commun.* **2016**, *7*, 11204.
- [49] K. Li, M. Han, R. Chen, S. L. Li, S. L. Xie, C. Y. Mao, X. H. Bu, X. L. Cao, L. Z. Dong, P. Y. Feng, Y. Q. Lan, *Adv. Mater.* **2016**, *28*, 8906–8911.
- [50] H. J. Lv, W. W. Guo, K. F. Wu, Z. Y. Chen, J. Bacsá, D. G. Musaev, Y. V. Gelettii, S. M. Lauinger, T. Q. Lian, C. L. Hill, *J. Am. Chem. Soc.* **2014**, *136*, 14015–14018.

---

Manuscript received: July 14, 2018

Accepted manuscript online: August 10, 2018

Version of record online: September 24, 2018